Surface-barrier and polarization effects in the photoemission from GaAs(110)

J. Henk* and W. Schattke
Institut für Theoretische Physik und Sternwarte, Christian-Albrechts-Universität, Leibnizstrasse 15, D-2300 Kiel, Federal Republic of Germany

H. Carstensen,† R. Manzke, and M. Skibowski
Institut für Experimentalphysik, Christian-Albrechts-Universität, Leibnizstrasse 19, D-2300 Kiel, Federal Republic of Germany
(Received 23 April 1992)

We have developed a theory of photoemission from III-V compound semiconductors within the one-step model and discuss the effect of transition-matrix elements, final states, and the surface barrier on the energy distribution of photoelectrons. As a prototype the (110) surface of GaAs is studied, and theoretical spectra are compared with experiment in normal as well as in non-normal emission. The specific position of the interface vacuum crystal, appearing in the calculation of the transition-matrix elements, influences the shape of the spectra considerably. The energy-distribution curves strongly depend on the escape angles of the photoelectrons as well as the incidence angles of the radiation leading to significant intensity variations especially of the dangling-bond surface state. Band-mapping methods prove to be misleading, in the worst cases by an error of about 100 meV in the estimation of the valence-band energies. The corrugated surface barrier is also investigated; our analysis favors a smooth saturated image potential barrier.

I. INTRODUCTION

Angle-resolved photoemission spectroscopy (ARPES) is by far the most important experimental tool for the determination of the electronic structure of semiconductors.[1] It affords knowledge about the bulk- and the surface-derived states throughout the whole Brillouin zone. Because the transitions take place between occupied and unoccupied wave functions the intensity of the detected photocurrent encloses information of both the valence-band and the conduction-band structure, thus complicating the interpretation of spectra without theoretical aid. Although the photoemission experiment is easily interpreted in terms of the direct-transition model, this detects only one part of the information comprised in the experimental data, especially in the case of semiconductors such as GaAs.

The usual procedure for treating experimental energy-distribution curves (EDC's) is smoothing followed by a deconvolution with simple profiles such as Gaussians or Lorentzians. Subsequently the energies of maxima and shoulders as a function of wave vector $\mathbf{k}$ are taken to obtain the dispersion relation of the electrons $E(\mathbf{k})$. A unique interpretation of the structures found in the EDC's is quite difficult without further theoretical guesses or band-structure calculations for both the initial-states and the final-states regime. The valence-band structure of all III-V compound semiconductors has been theoretically determined applying a lot of different approaches, whereas the conduction bands seem to be new ground, despite the existence of new powerful experimental tools such as the angle-resolved inverse photoemission spectroscopy. If a conduction-band structure calculation is not available one has to make more or less crude approximations, such as, e.g., free-electron parabolas. Assuming wave-vector-conserving transitions, i.e., direct transitions in the reduced zone scheme, so-called "band-mapping" methods may be applied to the experimental data successfully. With the use of structure plots most of the transitions can be related to specified valence and conduction bands.[2] The intensity of the photocurrent, however, is taken into account only qualitatively. For example, Huijser, van Laar, and van Rooy obtained the orbital composition of the dangling-bond surface state A_5 located at the outermost arsenic atoms on the (110) surface.[3] They notice that their findings reveal the shortcomings of the interpretation of experimental data with only one free-electron parabola as the final state. However, because of the large number of final-state bands the structure plots predict a lot of theoretically possible transitions, even if symmetry-selection rules discard a good deal of them. Due to matrix-element effects the number of experimentally observed transitions is usually much smaller [e.g., the work on GaAs(110), GaAs(001), and GaSb(001)(Refs. 4–6)], which calls for the discussion of the intensities.

Another difficulty is the separation of bulk-derived transitions from surface-derived transitions. Especially in the case of large unit cells this is a tough task because of the backfolding of the bulk bands, a special example being the spectra of GaAs(001).[5] This leads to a lot of nearly dispersionless structures in the EDC's which complicate the identification of the interesting surface-derived peaks, also additionally often characterized by

small bandwidths. A crucial test of a surface transition is to cover the crystal with a small amount of an adsorbate, e.g., oxygen. Because of the small escape depth of the photoelectrons the intensity of surface-derived structures dominates compared to that of the bulk-derived ones. The possible change in the geometry of the substrate forced by the adsorbates results in a different electronic structure of the outermost surface layers: on one hand the surface-derived peaks are shifted in energy, and on the other hand new adsorbate-induced peaks appear in the spectra. This may lead to a complex change of the shape of the EDC's complicating the distinction between surface and bulk states involved in the photoemission process. One argument often quoted is the following: surface states have to possess the periodicity of the surface, whereas bulk states may, but need not, show it. Especially if more than one surface Brillouin zone is detectable one traces the structures along $\mathbf{k}_{\parallel}$ and observes their dispersion leading to the desired distinction. Unfortunately the transition-matrix elements often suppress the intensity of some structures in some range of detection angles so that not all of the peaks can be observed throughout the Brillouin zones. Additionally, a comparably small dispersion of the peaks makes it harder to recognize the periodicity.[7] One further aid for the identification of surface peaks, i.e., the absence of dispersion in normal-emission spectra taken via scanning the photon energy, is obscured by emissions from band edges equally showing no dispersion.

The questions and statements raised above emphasize the necessity of calculations of the photoemission current within the one-step model, including correct transition matrix elements. The comparison of theory with experiment allows us to draw conclusions on the spatial distribution of both initial- and final-state wave functions, escape probabilities of the photoelectrons and, furthermore, to predict some free parameters inherent in the theory. The effect of surface states on the spectra may be easily analyzed because the surface could be eliminated in theory. Equipped with a computer program one is able to study selected effects on the spectra, for example, different surface-barrier shapes may be treated.

As a prototype we choose the (110) surface of GaAs which is partly well understood to date. There exist reliable models for the relaxation, favored by analyses of low-energy electron diffraction (LEED) by means of R-factors and total-energy calculations. Moreover, experimentally and theoretically determined valence-band structures compare very well. These are the reasons why this surface lends itself support for testing new theoretical concepts and sophisticated calculation schemes.[8] In the first stage of our study we have analyzed the photocurrent in the case of normal emission because most of the observed structures can be attributed to bulk transitions except one, which arises from the dangling-bond surface state. Therefore, the interpretation of the spectra is quite easy. While surface states are resonant with bulk states in the center of the Brillouin zone, they become more surface located in the rest of the $\mathbf{k}_{\parallel}$ space. For instance, some of them are lying in the bulk band gap and are strongly located at the first few layers. In the second stage, i.e., the case of non-normal emission, we have confined ourselves to study polarization effects on the EDC's. The electron density of the dangling-bond state is clearly located at the outermost surface layer and directed to the vacuum at an angle of about 45° with respect to the surface normal.[9] The intensity varies drastically if the direction of the incident radiation and the escape angle of the detected photoelectrons are changed.[3,10]

In a previous paper on GaAs(110) (Ref. 4) we have shown that all peaks in the experimental EDC's in normal emission could be explained using structure plots, i.e., for lower photon energies the direct-transition model yielded an agreement from very close to a few 0.1 eV. The one-dimensional density of states showed to be less important. The direct comparison of the theoretical and experimental intensities was encouraging, but there still remained clear differences, demonstrating that the conformity within the energy positions did not establish a similar quality of the matrix-element calculation. In the integration of the matrix elements we had neglected the boundary condition of the final state, i.e., the final-state wave function was extrapolated into the vacuum region. Sufficient convergence of the integration was assured by the localization of atomic orbitals, into which the initial states are expanded. The correct boundary, however, was incorporated in those parts of the calculation where the individually weighted final-state bands, which contribute to the outgoing LEED wave, were summed up. In this paper we especially investigate the effect of those surface properties on the matrix elements. The integration is separated into a crystal and vacuum part and is carried out with the correct representation of the final state within the respective region. This procedure increases the necessary CPU time significantly. Additionally, we discuss the influence of several shapes of the surface-barrier potential on the EDC's.

The paper is organized as follows. In Sec. II we give a short explanation of the theoretical framework, especially the calculation of the initial states, the final state, transition-matrix elements, and the inclusion of the corrugated surface barrier. Subsequently we report some results for emission along the surface normal, before turning to the case of non-normal emission. In the latter we treat escape angles corresponding to values of the wave-vector component parallel to the surface near the symmetry point $\overline{X}'$. We finish the discussion with a study of the effect of the surface barrier on the energy-distribution curves in non-normal emission. In the appendixes sketches of our computer-program package for the photoemission calculations and the estimation of the matrix elements are given.

II. THEORY

In this section a short summary of the theory we adopted for the photoemission from III-V compound semiconductors is given.

A. Photoemission

The starting point is the "golden-rule" formulation of the photoemission process as derived by a lot of authors;

see, for example, Feibelman and Eastman.[11] Within the one-step model the differential photocurrent $I(E,\vartheta,\varphi)$ may be written as

$$I(E,\vartheta,\varphi) \propto \sqrt{E_{\rm kin}} \sum_i |\langle \Phi^*_{\rm LEED}(\mathbf{k}_\parallel)|D|\Phi_i(\mathbf{k}_\parallel)\rangle|^2 \times \delta(E-E_i-\hbar\omega), \quad (1)$$

where the sum runs over all initial states Φ_i with energy E_i. The final state $\Phi^*_{\rm LEED}$ is the time reversal of a LEED state, i.e., the wave function one would use to describe a low-energy electron-diffraction experiment.[12] Its energy is $E_i+\hbar\omega$ with $\hbar\omega$ denoting the photon energy. The escape angles ϑ and φ and the kinetic energy $E_{\rm kin}$ determine the surface parallel component of the wave vector by

$$\mathbf{k}_\parallel = \sqrt{2mE_{\rm kin}/\hbar^2}\,\sin\vartheta \begin{pmatrix}\cos\varphi\\ \sin\varphi\end{pmatrix}. \quad (2)$$

The dipole operator may be written as the inner product of the vector potential $\mathbf{A}$ and the momentum operator $\mathbf{p}$, $D=\mathbf{A}\cdot\mathbf{p}$.

Using Dirac's identity the photocurrent can be expressed in the form

$$I(E,\vartheta,\varphi) \propto -\sqrt{E_{\rm kin}}{\rm Im}\sum_{ij} M(i)\,\tilde{G}_{ij}(E+i\eta)\,M(j)^*, \quad (3)$$

where $M(i)$ denotes the transition-matrix element between the time-reversed LEED state and initial state Φ_i. Because the initial states may be nonorthonormal the Green's function $\tilde{G}$ of the semi-infinite crystal is given in a conjugate basis set, which we denote by a tilde. The parameter η represents the hole-lifetime broadening. To simulate many-particle effects an optical potential is introduced. Its imaginary part, ${\rm Im}V_{\rm opt}$, determines the finite lifetime of the excited states. We use the following energy dependence:

$${\rm Im}V_{\rm opt}(E) = \frac{c}{1+\exp[-(E-\mu)/b]} + a, \quad (4)$$

which has been applied successfully in the photoemission theory[4,13] and in a recent theoretical analysis of total current spectra (TCS) from GaAs(110).[14] The plasmon energy is represented by μ, the real part of the optical potential is set to zero.

B. Initial states

We calculate the initial states by the empirical tight-binding method (ETBM) as formulated in the extended Hückel theory (EHT). Our basis set consists of the $4s$ and the $4p$ atomic orbitals of gallium and arsenic,[15] and we take into account interactions including orbitals located at third-nearest-neighbor atoms. The EHT formula for nondiagonal elements of the Hamiltonian matrix, i.e., for $(\alpha l)\neq(\beta m)$, reads

$$H_{\alpha l\beta m}(\mathbf{k}) = -\frac{K_{\alpha\beta}}{2}\,(I_{\alpha l}+I_{\beta m})\,S_{\alpha l\beta m}(\mathbf{k}), \quad (5)$$

and for diagonal elements we write

$$H_{\alpha l\alpha l}(\mathbf{k}) = -\tilde{I}_{\alpha l} - K_{\alpha\alpha}I_{\alpha l}[S_{\alpha l\alpha l}(\mathbf{k})-1]. \quad (6)$$

Here, α and β label the orbitals of the basis atoms l and m. The overlap matrix is denoted S. The parameters $K_{\alpha\beta}$ only depend on the angular momentum of the orbitals so that we are concerned with three different values, i.e., K_{ss}, K_{sp}, and K_{pp}. The remaining quantities $I_{\alpha l}$ and $\tilde{I}_{\alpha l}$ represent the orbital energies. The 11 EHT parameters are determined by fitting the bulk valence-band structure to that calculated by Chelikowsky and Cohen.[16] Additionally, we have calculated the charge transfer via Mulliken's population analysis[17] yielding a transfer of 0.297 electrons from Ga to As. This agrees quite well with the Phillips ionicity, which for GaAs is 0.310.[18] Therefore, the dispersion of the electronic states as well as the wave functions themselves seem to be described correctly within our approach. The EHT scheme may be easily extended to self-consistency,[19] which, however, is not our purpose in this paper. In fact we have performed a self-consistent calculation of the valence bands along those lines.[20] The parameters of a slightly enhanced basis set converged in the self-consistency loop to values comparable with the fitted quantities used here. The small differences are attributed to shortcomings of that procedure enforced by the EHT parametrization. Thus, we believe that the quality of the wave functions should not suffer from the further fit to a standard band structure; our valence bands should represent an acceptable approximation.

In Fig. 1 the resulting bulk-valence-band structure is

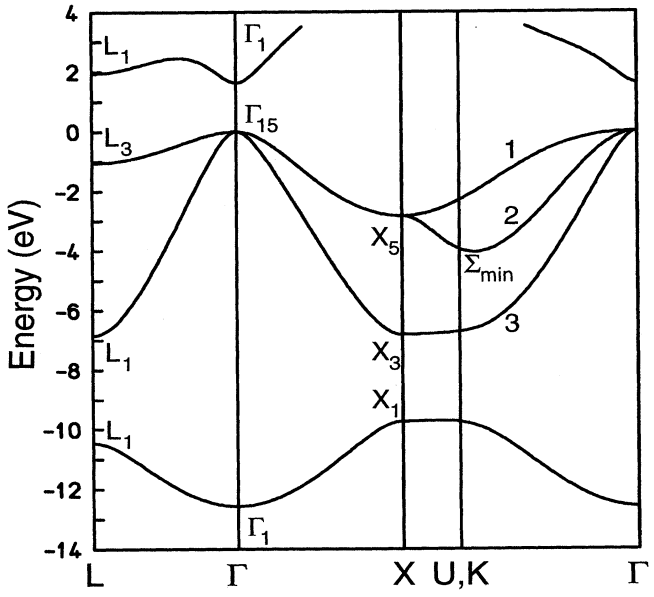

FIG. 1. Valence-band structure of GaAs calculated within the EHT scheme. The energy bands are shown along the high-symmetry lines of the bulk Brillouin zone. At band edges and points of high symmetry the group representation is specified. Additionally, along the direction Σ (Γ–K, U–X) some bands are labeled with numbers. The energy zero refers to the valence-band maximum.

shown. It compares very well with that calculated by Chelikowsky and Cohen[16] and that of Cardona, Christensen, and Fasol.[21]. The relevant direction of high symmetry for emission normal to the (110) surface is the line Γ–Σ–X. The uppermost band dispersing down from Γ_{15} to X_5 possesses Σ_2 symmetry, while the others show Σ_1 symmetry. For better identification they are marked with increasing numbers from the valence-band maximum down to lower energies.

The electronic structure of the semi-infinite solid is calculated within the Green's-function approach applying a highly convergent renormalization scheme proposed by López Sancho, López Sancho, and Rubio.[22] This "layer-doubling" procedure enables us to determine the Green's function of the whole truncated crystal by means of transfer matrices, the Green's function given in the basis of layer Bloch sums $\mid p, \mathbf{k}_\parallel, \alpha, l\rangle$, which are indexed by the crystal layer p and the orbital α of atom species l. A determination of the bulk resolvent is not necessary.[23] As our basis set consists of nonorthonormal atomic wave functions we are forced to introduce a conjugated basis, which, however, does not enter the calculations explicitly.[24] Because of the good convergence behavior we are able to treat surfaces with large unit cells within moderate computer time. For example, with a hole-lifetime broadening of $\eta = 0.05$ eV no more than seven iterations are needed to give the Green's functions of the bulk, the ideal surface, and of the reconstructed surface. The final interactions between two stacks of renormalized layers are reduced to less than 1% of the initial layer interactions. Our tight-binding model has proven its suitability for GaAs(111)2×2,[25] GaAs($\overline{1}\overline{1}\overline{1}$)2×2, and GaAs(001),[26] essentially reproducing the experimental peak positions in a band-mapping procedure.

There exist a lot of relaxation models for the (110) surface of GaAs which are quite similar. As in our recent study of the photoemission current of GaAs(110) (Ref. 4) we use the one proposed by Duke *et al.*,[27] which is confirmed by a LEED R-factor analysis. The resulting surface-band structure compares very well with that derived by Zhang and Cohen applying the self-consistent local-density approximation in a slab geometry.[28] There exists one interesting deviation between other theoretical surface-band structures and ours. In our work the A_5 surface state is lying at -0.05 eV in the center of the surface Brillouin zone, whereas in other sophisticated slab calculations its energy is distinctly lower, e.g., -0.8 eV to -0.4 eV.[29] As in the case of GaSb(110) (Ref. 30) the dangling bond is found near the VBM in experiment,[4] but shows only a weak structure in the EDC's due to its resonant behavior. At this point an advantage of the semi-infinite model over a slab calculation, where resonant states localized on opposite surfaces cannot be decoupled, is revealed. Clearly, the better agreement of A_5 with experiment is more suitable as the basis of a calculation of photoemission intensities even if it is not so well founded like a self-consistent calculation.

C. Time-reversed LEED state

The initial states may be very well described within a localized orbital basis. For the description of the final state of photoemission, i.e., the time-reversed LEED state, a plane-wave basis is more appropriate because of its similarity to free electrons.

In the vacuum region, $\{z \geq z_0\}$, the potential vanishes, assuming a steplike surface barrier, and the final state may be written as

$$\Phi^*_{\mathrm{LEED}}(\mathbf{k}_\parallel, E) = \exp(i\mathbf{k}_\parallel \cdot \boldsymbol{\varrho} + i\kappa_0 z) + \sum_{\mathbf{g}} \varphi^*_{\mathbf{g}} \exp[i(\mathbf{k}_\parallel + \mathbf{g}) \cdot \boldsymbol{\varrho} - i\kappa^*_{\mathbf{g}} z], \tag{7}$$

where the first term represents the incoming (0,0)-LEED beam, whereas the remaining sum runs over all backscattered beams with amplitudes $\varphi_{\mathbf{g}}$ enumerated by surface reciprocal-lattice vectors. The latter may not leave the crystal depending on energy and escape angles. $\boldsymbol{\varrho}$ is a vector parallel to the surface plane, $\boldsymbol{\varrho} = (x, y)$. The x axis points into the $[1\overline{1}0]$ direction, whereas the y axis points into the [001] direction. A mirror plane of the (110) surface is formed by the x-z plane. This system of coordinates is used throughout in this paper. The wave-vector component perpendicular to the surface $\kappa_{\mathbf{g}}$ is given by

$$\kappa_{\mathbf{g}} = \sqrt{\frac{2m(E - \Phi_{\mathrm{th}})}{\hbar^2} - (\mathbf{k}_\parallel + \mathbf{g})^2}, \tag{8}$$

the energy E taken relative to the VBM. If the radicand is negative, $\kappa_{\mathbf{g}}$ is purely imaginary describing damped plane waves in the direction towards the vacuum. κ_0 corresponds to the lattice vector $\mathbf{g} = (0, 0)$. The photoemission threshold Φ_{th}, e.g., the energetic difference between the vacuum level and the VBM, is set to 5.25 eV in accordance with theoretical and experimental estimations.

In the crystal region, $\{z \leq z_0\}$, the final state is expanded into solutions Ψ_i of the bulk Schrödinger equation,

$$\Phi^*_{\mathrm{LEED}}(\mathbf{k}_\parallel, E) = \sum_i t^*_i(\mathbf{k}_\parallel, E)\ \Psi^*_i(\mathbf{k}_\parallel, k^{(i)}_\perp, E). \tag{9}$$

The expansion coefficients t_i and $\varphi_{\mathbf{g}}$ are fixed by the condition that the final-state wave function and its derivative normal to surface are continuous across the surface $\{z = z_0\}$. In the considered energy range 27 surface reciprocal-lattice vectors are taken into account leaving the mismatch in both the wave function and its derivative less than 2%. Because the final state is totally symmetric[31] wave functions with Σ_2 symmetry do not couple to the outgoing wave.

The bulk states Ψ_i are computed within the empirical pseudopotential method (EPM) applying the local potential of Cohen and Bergstresser,[32] which has been evaluated by fitting to optical data near the fundamental band gap. The wave functions are given in a plane-wave expansion,

$$\Psi_i(\mathbf{k}^{(i)}) = \sum_{\mathbf{G}} \alpha^{(i)}_{\mathbf{G}}(\mathbf{k}^{(i)}) \exp[-i(\mathbf{k}^{(i)*} + \mathbf{G}) \cdot \mathbf{r}] \tag{10}$$

with $\mathbf{k}^{(i)} = (\mathbf{k}_\parallel, k_\perp^{(i)})$. In the computation 137 bulk reciprocal-lattice vectors $\mathbf{G}$ are taken into account. To include the surface in the calculations we have to follow the concept of Heine's complex band structure.[33] Because we need the wave functions for given energy and $\mathbf{k}_\parallel$ we utilize a simple computational scheme by Pendry, which determines the coefficients $\alpha_{\mathbf{G}}^{(i)}$ and the components of the complex wave vector $k_\perp^{(i)}$ directly.[34]

In Fig. 2 the complex band structure for the symmetry direction Σ together with the expansion coefficients t_i of the final state Φ_{LEED} is shown. Because of the nonvanishing imaginary part of the optical potential the band gaps, which would occasionally occur, are bridged over. As in the photoemission calculations presented below the parameters of the energy dependence are chosen as $a = -0.3$ eV, $b = 2.5$ eV, $c = -1.5$ eV, and $\mu = 17.0$ eV, cf. Eq. (4). E.g., at lower energies bands 5 and 6 behave like imaginary bands of the first kind connecting real bands.[35] At higher energies the imaginary part of $k_\perp$ generally slightly increases because of the high damping above the plasmon energy. Furthermore, the bands are similar to free-electron parabolas, but possess different slopes. As expected earlier[4] conduction band 7 couples very strongly to the outgoing wave as can be seen by the respective expansion coefficient. The corresponding wave function describes electrons propagating normal to the surface as it becomes evident from the plane-wave

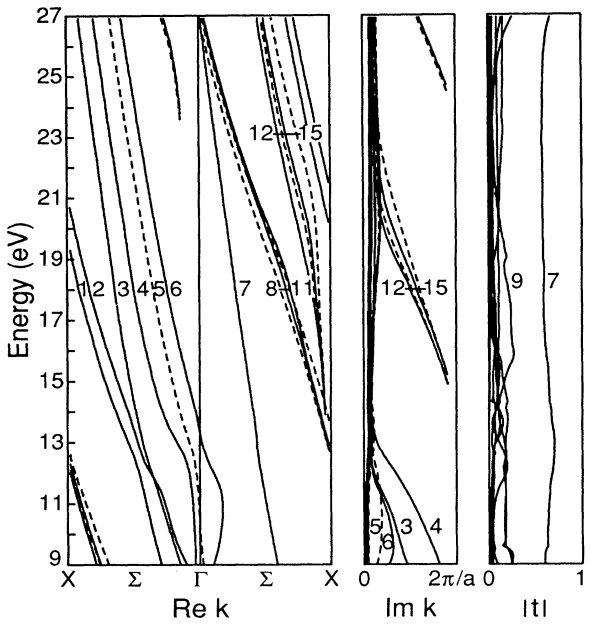

FIG. 2. Complex conduction-band structure of GaAs for the symmetry direction Σ calculated within the EPM scheme. In the left and the middle inset the real part of $k_\perp$ and its imaginary part are shown. Only bands with damping less than $2\pi/a$ are presented. Σ_2 states are specified by dashed lines, Σ_1 states by solid lines. In the right part the expansion coefficients t_i of the photoemission final state are drawn, labeled the same way as the corresponding bands. Energy zero refers to VBM.

expansion. The dominating contribution arises from that plane wave with the shortest umklapp perpendicular to the surface; the remaining are by far smaller, a result which is sometimes stated.

A problem worth mentioning arises by the use of two different Hamiltonians, one for the valence-band states and the other for the conduction-band states. In other calculation schemes, based on the computer program PEOVER,[36] the initial and the final states are calculated by the layer-KKR method. The problem is to get the appropriate KKR potential in the case of covalent binding, if there is any. An example avoiding this difficulty is a computer program calculating the initial states in the tight-binding approach and the final states via the layer-KKR method, which is applied successfully to layered crystals.[37] To analyze the question whether the EPM and the ETBM Hamiltonian represent the same operator, we have compared the bulk-band structure and the total valence-charge density determined within both approaches, EPM and ETBM. We find a quite good agreement of the band structures; the pseudopotential bands show less dispersion than the ETBM bands, which we attribute to neglecting nonlocal parts of the pseudopotential. The charge densities compare quite well, too. One has to exclude the core region keeping in mind that in the EPM case the charge density is determined by the pseudowave functions instead of the still unknown true ones. The former are quite smooth in the core region, whereas the latter show rapid oscillations, as they do in the ETBM case.[15] Additionally, the Hamiltonian operators may be compared directly by transforming the EPM-Hamiltonian matrix into a tight-binding representation.[38] The quantity $H_{\alpha l \beta m}(\mathbf{k})/S_{\alpha l \beta m}(\mathbf{k})$ shows a very similar behavior in the reciprocal space for both calculation methods. This confirms our EHT formulas, Eqs. (5) and (6): for the nondiagonal elements H/S is constant by definition in the EHT case and shows to be nearly constant in the EPM case. If one uses the original EHT formula for the diagonal matrix elements, which reads $H_{\alpha l \alpha l} = -I_{\alpha l}$, the agreement between both approaches is not as good as with the use of our formula, which, however, introduces four additional parameters $\tilde{I}_{\alpha l}$ to be fitted. As we see, this total agreement justifies the application of those Hamiltonians in our photoemission calculations.

D. Transition-matrix elements

Because of the small escape depth of the photoelectrons the spatial variation of the electromagnetic field is neglected in the energy range concerned. However, its diffraction at the surface is included via Fresnel's formulas. The transition-matrix elements of Eq. (3) have to be calculated between the time-reversed LEED state Φ_{LEED}^* and layer-Bloch sums indicated by the layer p, $\mathbf{k}_\parallel$, and the orbital α located at atoms of species l,

$$M(p, \mathbf{k}_\parallel, \alpha, l) = \langle \Phi_{\mathrm{LEED}}^* | D | p, \mathbf{k}_\parallel, \alpha, l \rangle. \tag{11}$$

The integration has to be extended over the whole space. Because the final state is differently expanded in the

vacuum and in the crystal region, cf. Eqs. (7) and (9), the total matrix element is divided into two terms, $M_v(p, \mathbf{k}_\parallel, \alpha, l)$ and $M_c(p, \mathbf{k}_\parallel, \alpha, l)$, where the quadrature is restricted to the vacuum (v) and to the crystal (c), respectively.

Firstly, we treat the crystal part of the matrix element. Inserting the expressions for the final state and the Bloch sum results in a summation over all reciprocal bulk lattice vectors, final states, and layer unit cells. The assumption of translational invariance parallel to the surface results in the conservation of the parallel component of the wave vector $\mathbf{k}_\parallel$ modulo in-plane reciprocal-lattice vectors. The remaining quadrature is a Fourier transformation of the atomic orbital $\Phi_{\alpha l}$ restricted to the specified volume,

$$F_{\alpha l}(z_0, \mathbf{k}) = \int_{\mathcal{R}^2 \times [-\infty, z_0]} e^{i\mathbf{k}\cdot\mathbf{r}}\, \Phi_{\alpha l}(\mathbf{r} - \mathbf{R})\, dr^3. \qquad (12)$$

This is solved analytically; however, the derivation of the resulting formulas is straightforward but tedious. Examples are shown in Appendix B. In our previous work[4] we had to require that the plane wave with its complex wave vector does not increase stronger than the atomic orbital decreases in order to arrive at convergence. As could be seen in Fig. 2, rapidly increasing final states do not couple strongly to the outgoing wave, and therefore this has been a principal but no practical shortcoming in the calculations. Due to the surface cutoff at z_0 this requirement is no longer necessary.

To treat the vacuum part of the matrix element we can use the previous results. The only differences are that now the sums occurring from the expansion of the final state and the layer-Bloch sums run over the reciprocal surface vectors instead over bulk reciprocal ones and that the integration is over the vacuum half-space. The latter can be solved immediately: the Fourier transform of the atomic orbital restricted to the vacuum is just that over the whole space minus that restricted to the crystal volume. The transition-matrix elements in the approximation of neglecting the surface have been evaluated by Gadzuk.[39]

The Fourier transforms depend on the location of the atomic wave function perpendicular to the surface. This leads to a strong modification of the transition-matrix elements of surface-located Bloch sums compared to those of bulk-located Bloch sums. As an example we show in Fig. 3 the Fourier transformed 4s orbital of gallium, where the quadrature is restricted to the crystal according to Eq. (12). For small values of z_0 the Fourier transform equals nearly to zero, whereas for large values of z_0 it becomes also constant reaching the bulk value at $z_0 \approx 2.5a/4$, $a = 5.632\,65$ Å being the bulk lattice constant (the layer spacing is $1.42a/4$). In the intermediate region, $-2a/4 \le z_0 \le 2a/4$, the real part increases rapidly from zero to the bulk value while the imaginary part shows a distinct maximum at $z_0 = 0$. It is evident from our analysis that a change of the parameter z_0 effects the resulting EDC's considerably, which we shall show below.

Because of the small escape depth photoemission spectroscopy is very sensitive to surface transitions. In theory this feature can be seen by plotting the modulus of transition-matrix elements with respect to the crystal layer as done in Fig. 4. First of all, one observes an exponential-like decay of the matrix elements. At the surface region, i.e., the outermost six layers, strong deviations from this global behavior due to the surface cutoff and the relaxation occur. Note that matrix elements of s orbitals are much smaller than that of p orbitals.

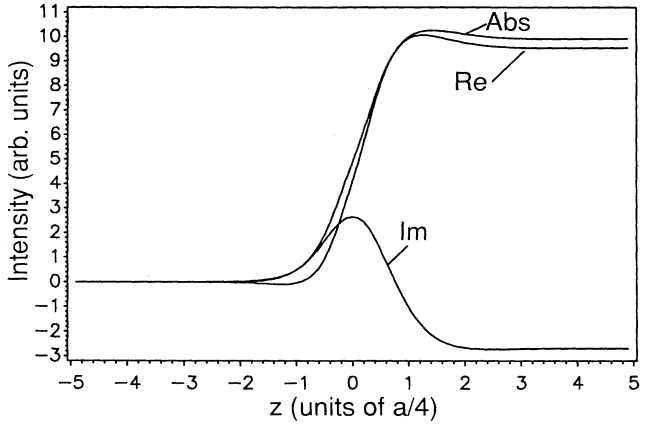

FIG. 3. Fourier transform of a gallium 4s wave function located at the origin $z = 0$. The quadrature is restricted to the half-space $\{z \le z_0\}$. The wave vector chosen is $\mathbf{k} = (0.2, 0.2, 0.8 - 0.3i)2\pi/a$. The real part is denoted "Re," the imaginary part by "Im," and the modulus by "Abs."

The transition-matrix elements are a substantial part of the theory because they govern the intensity of the photocurrent. The numerical effort is considerable but far-going approximations, which allow calculations of intensities without taking into account transition-matrix elements or the surface, e.g., angle-resolved initial state spectra[40] or the theory derived by Humphreys, Srivastava, and Williams[41] have to pay with a rather limited

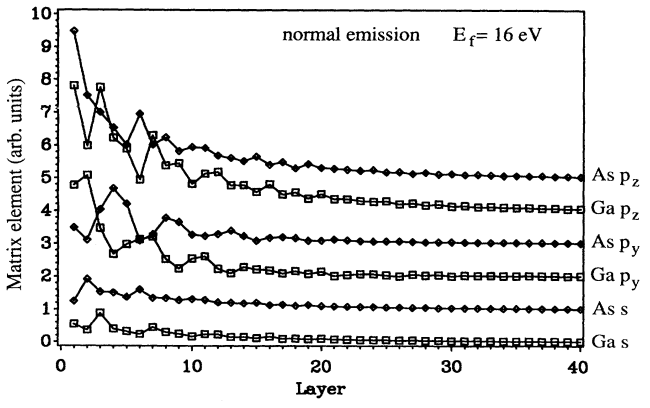

FIG. 4. Modulus of transition-matrix elements vs crystal layer. The final-state energy is 16 eV, $\mathbf{k}_\parallel$ being zero. The incidence angles of the radiation are $\vartheta_A = 45°$ and $\varphi_A = 270°$ ($\tilde{p}$ polarization). The interface plane solid vacuum lies at $z_0 = 3.19a/4$. The orbital type is shown on the right. Ga and As curves are labeled with squares and diamonds, respectively. The value of each curve at layer 40 represents its approximately zero ordinate.

range of applicability in describing the spectra. In the latter the transition-matrix elements show nearly no effect on the EDC's contrary to our findings.

E. Surface barrier

In photoemission spectroscopy the excited electrons are propagating through three different kinds of regions. Firstly, they have to pass the bulk with the strong potential giving rise to the band structure. Secondly, at the interface region between the solid and the vacuum the electrons may be scattered back from the surface barrier and additionally feel the long-range Coulombic image state potential outside the crystal. In the third region far outside the crystal the potential is very small compared to that of the former regions and therefore may be asymptotically neglected, i.e., it is set to zero as the starting value in the integration of the Schrödinger equation from outside towards the interior of the solid.

At higher kinetic energies the effect of the surface barrier may be neglected but at lower kinetic energies the photoelectrons are influenced strongly. Therefore, the shape of the barrier potential may be evaluated by comparing theoretical EDC's calculated for a variety of barrier shapes with experimentally determined spectra.

In the interface region the crystal potential is not periodic perpendicular to the surface, consequently no Bloch condition can be employed. By application of the propagator formalism this difficulty has been overcome.[42] Both the wave function and the potential are given in a mixed representation, i.e., a Fourier decomposition parallel to the surface with the Fourier coefficients depending on the coordinate perpendicular to the surface z. Then we get for the potential V in the interface region

$$V(\varrho, z) = \sum_{\mathbf{g}} V_{\mathbf{g}}(z) \exp(i\mathbf{g} \cdot \varrho), \tag{13}$$

ϱ being a vector parallel to the surface. In a similar way the wave function Ψ is written for fixed energy E and $\mathbf{k}_{\|}$,

$$\Psi(\varrho, z) = \sum_{\mathbf{g}} \phi_{\mathbf{g}}(z) \exp[i(\mathbf{k}_{\|} + \mathbf{g}) \cdot \varrho]. \tag{14}$$

Taking into account n surface-reciprocal-lattice vectors $\mathbf{g}$ a vector $\mathbf{\Psi}$ may be introduced, the first n components given by the coefficients $\phi_{\mathbf{g}}$ and the second n components by their derivatives with respect to z. Thus, the Schrödinger equation becomes a first-order system of $2n$-coupled differential equations. The propagator matrix $P(z, z')$ is defined by the relation

$$\mathbf{\Psi}(z') = P(z', z)\mathbf{\Psi}(z) \tag{15}$$

and thus satisfies the equations

$$P(z, z') = P(z, z'')P(z'', z'), \forall z'', \tag{16}$$

$$P(z, z) = 1, \tag{17}$$

1 denoting the unit $2n \times 2n$ matrix. The propagator matrix can be calculated by direct integration of the Schrödinger equation. In our theory the application of the propagator formalism influences only the expansion coefficients t_i and $\varphi_{\mathbf{g}}$ of the time-reversed LEED state. Firstly, we compute the propagator P from the vacuum region far enough outside the crystal to the third, unrelaxed crystal layer. Subsequently the coefficients are determined by the usual matching condition. The transition-matrix elements are calculated in the way described before. In principle, one has to calculate also the matrix elements between the initial states and the true final wave function given in the mixed representation, i.e., including the transition region composed of the first two layers and the surface barrier. This problem might be tackled in the future. Here, we replace for the calculation of the matrix elements the transition region by an ideal separating plane at position z_0, which is treated as a fit parameter.

The corrugated barrier potential is determined by the Fourier coefficients $V_{\mathbf{g}}(z)$ of the mixed representation. For $\mathbf{g} \neq 0$ these decrease rapidly, whereas for $\mathbf{g} = 0$ it increases to the step height with increasing z outside the crystal. In the interior the surface potential fits to the known bulk pseudopotential used in the EPM calculations. A lot of different models for the barrier shape have been suggested for metals,[43] but in the case of semiconductors only a little work on this topic has been published. In a self-consistent calculation within the nonlocal-density approximation of the density-functional theory Manghi has calculated the electronic structure of the GaAs(110) surface and has given a detailed analysis of the barrier shape.[44] As in the case of metals one observes a saturated image-potential barrier with a nearly linear ascent.

In order to reproduce the barrier shape determined by Manghi we have used the following parametrization of the barrier.[45] For $\mathbf{g} = (0, 0)$ the Fourier coefficient reads

$$V_0(z) = \begin{cases} \frac{1}{4(z_{\mathrm{im}} - z)}, & z \geq z_v \\ \frac{a}{1 + b(z - z_c)^2} + c, & z_v \geq z \geq z_c. \end{cases} \tag{18}$$

The adjustable parameters are z_v and z_c, the boundaries of the barrier towards the vacuum and towards the outermost surface layer, respectively, and z_{im} is the pole of the image potential. The values of a, b, and c are fixed by continuity at z_c and smooth continuity at z_v. For nonvanishing surface-reciprocal-lattice vectors we assume a decay like a Gaussian with parameter λ,

$$V_{\mathbf{g}}(z) = V_{\mathbf{g}}(z_c) \exp[-\lambda(z - z_c)^2], \quad z \geq z_c. \tag{19}$$

The imaginary part of the optical potential is taken as spatially constant throughout the whole bulk crystal and decays like a Gaussian with the same parameter λ. Using this parametrization we are able to represent a lot of different shapes; for example, we have studied a sharp step and very smooth interpolating forms. The main attributes that remain unchanged are the long-range Coulomb image potential and the nearly linear interpolant in the intermediate region.

III. EXPERIMENT

In this section a short summary of the experiment is given. We rely on data from an experiment described in a

recent paper.[4] Only the main features are repeated. The experimental spectra have been taken with synchrotron radiation in the energy range from 10 eV up to 30 eV and optional with unpolarized He I radiation. The energy resolution has been chosen to 100 meV and the angle resolution has been better than 0.5°. In normal emission the angle of incidence is 45° with respect to the surface normal, the dominant component of the vector potential **A** as well as the plane of incidence lying in the mirror plane of the (110) surface. In non-normal emission the EDC's have been taken at various angles and polarization conditions. For comparison with theory the experimental data have been slightly smoothed after subtracting the inelastic background.

IV. DISCUSSION AND RESULTS

A. Normal emission

In the analysis of normal-emission spectra from GaAs(110) one is concerned with the high-symmetry line Σ of the bulk Brillouin zone. Because the final state is totally symmetric[31] only bulk states with even parity, i.e., Σ_1 symmetry, couple to the outgoing wave. Using p-polarized light, the vector potential lying in the mirror plane of the surface, only Σ_1-symmetry initial states contribute to the photocurrent, whereas with s-polarized light only the odd states are detected. Because the experimental data have been taken with $\tilde{p}$-polarized light ($\varphi_{\mathbf{A}} = 270°$, **A** denoting the vector potential) we confine our analyses to that case. In all theoretical EDC's presented in this subsection the surface barrier with a shape determined by Manghi[44] is included.

At first, we discuss the effect of free parameters in the theory on the calculated EDC's before we compare our results with the experiment. As it is evident from Fig. 3 the coordinate z_0 of the interface vacuum crystal regarded relative to an atomic plane considerably influences the Fourier transforms of the atomic wave functions, which are an essential part of the transition-matrix elements. As one example we show in Fig. 5 25-eV spectra for various values of z_0, see also Eq. (12). The salient feature is the ratio of the intensity near the VBM to that at -2.8 eV, being the energy of the X_5 point. At smaller values of z_0, i.e., $2.94a/4$ and $3.44a/4$, the latter peak is dominating the EDC's. At large values the VBM shows the by far highest intensity, whereas at the intermediate value $3.69a/4$ both transitions possess nearly the same intensity. As in experiment the intensity at initial energies less than -4.5 eV is mostly suppressed. The comparison with the experimental EDC reveals that the theoretical spectrum for $z_0 = 3.69a/4$ results in the best agreement. Note that this value for z_0 coincides nearly with that of the half-step height of the saturated image potential barrier, or in other words, it lies in a distance from the uppermost atomic plane somewhat greater than one-half of the interlayer spacing, as is evident from Fig. 10. The correspondence between theory and experiment is quite good. All relevant features are reproduced by the theory, except the strong intensity at energies between -2.0 eV to -0.8 eV, which are due to transitions from initial state 3 into final states 9 and 11. This lack may be attributed to the uncertainties in the EPM conduction-band structure. Because of the large computer time necessary for the computation of one spectrum we did not regard it worth fine tuning z_0 for best agreement.

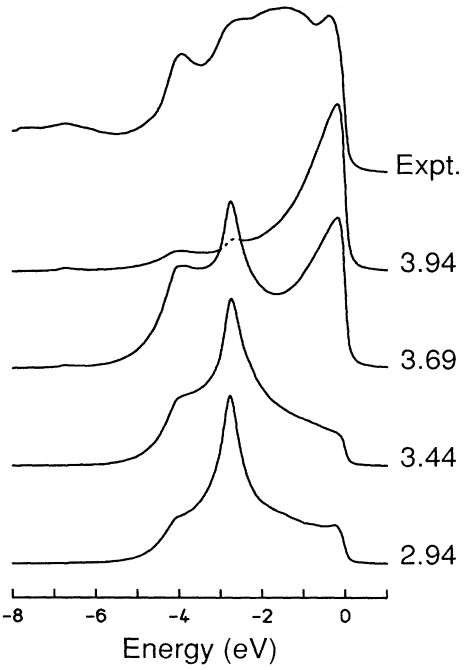

FIG. 5. Theoretical energy-distribution curves for various values of z_0 compared with an experimental spectrum. The former are indicated by z_0 in units of $a/4$, the origin located at the third, unrelaxed crystal layer, the latter is labeled "Expt." The photon energy is 25 eV and $\tilde{p}$ polarization is assumed. Initial energy refers to VBM.

As a second example we analyze the polarization dependence of the theoretical EDC's. Using p-polarized radiation the photons impinge in the direction of the unoccupied gallium-derived dangling-bond surface state C_3 onto the surface ($\varphi_{\mathbf{A}} = 90°$). Under $\tilde{p}$-polarization conditions they point into the direction of the occupied dangling bond A_5 ($\varphi_{\mathbf{A}} = 270°$); in both cases the vector potential **A** is lying in the mirror plane of the (110) surface. In Fig. 6 we show the theoretical EDC's calculated with $z_0 = 3.69a/4$. In the energy range from -2.8 eV up to the VBM one observes only small changes due to the polarization at 17-eV photon energy. Near the VBM a small maximum occurs attributed to the surface state A_5, its energy being -0.05 eV. Contrary to expectation the emission seems to be more pronounced in the case of $\tilde{p}$ polarization where the field vector **A** is nearly perpendicular to the dangling-bond orbital. This underlines the shortcomings of a purely atomic point of view of the photoemission process. At about -4.0 eV the spectrum for $\tilde{p}$ polarization shows a distinct minimum, whereas in the other case, i.e., p-polarized radiation, a maximum occurs. The peak at -5.6 eV, which is due to transitions from initial state 3 into final state 7, cf. Figs. 1 and 2, is lower for p polarization. Emissions from the band edge $\Sigma_{\min}$ at -4.0 eV visible for photon energies above 21 eV

are stronger in the case of $\tilde{p}$ polarization than for p polarization, which may be connected to final states with nonvanishing parallel wave-vector component. The initial state is mainly built by the p_z orbitals of arsenic and gallium, contributions from p_y orbitals are smaller by a factor of about 2.

In Fig. 7 we present a complete series of theoretical and experimental EDC's taken at various photon energies. The calculations have been performed with $z_0 = 3.69a/4$ and $\tilde{p}$-polarized radiation. One observes that emissions at -6.8-eV initial energy, referring to the X_3 point, are almost suppressed over the whole photon-energy range in theory as well as in experiment. The initial states at that energy are mainly built by the s orbitals of gallium, leading to comparably small transition matrix elements, cf. Fig. 4. In the experimental EDC's the transitions from initial states 2 and 3 into final state 7 dominate, which we attribute to the strong coupling of that final state to the outgoing wave. Especially at 19- and 20-eV photon energy the intensity at about -2.0 eV is emphasized. At higher excitation energies, i.e., from 21.2 eV up to 23 eV, it is suppressed. This feature is well reproduced by the theory. At 28-eV photon energy the spectra show at the VBM one dominating peak and additional weak shoulders and maxima at the energies of the bulk band edges. This is explained by final-state effects: at that energy a lot of direct transitions near the center of the bulk Brillouin zone take place leading to this immense intensity. Furthermore, due to the strong damping the conservation of $k_\perp$ is not as exact as at lower final-state energies, thus one observes only significant structures at the energies of band edges.

Although theory and experiment compare well, some differences are present. As an example, the main intensity at 21.2-eV photon energy arises from the peak at -4.5-eV inital energy in the experimental EDC, whereas in theory the main maximum lies at -2.8 eV. On the one hand the conduction-band structure includes some uncertainties, which are due to the pseudopotential parameters. These have been evaluated by fitting optical data in the energy range near the fundamental band gap, whereas we are concerned with higher energies. However, in favor of that calculation a conduction-band structure calculated recently with the layer-KKR method[14] differs only slightly in the VUV energy range. On the other hand, the influence of the matrix elements in dependence of the detailed surface properties seems to be important. Generally, however, it can be stressed that the overall agreement between theory and experiment has improved considerably in comparison with the former calculation.[4]

B. Non-normal emission

In the center of the surface Brillouin zone surface states are resonant with bulk states leading to transitions with

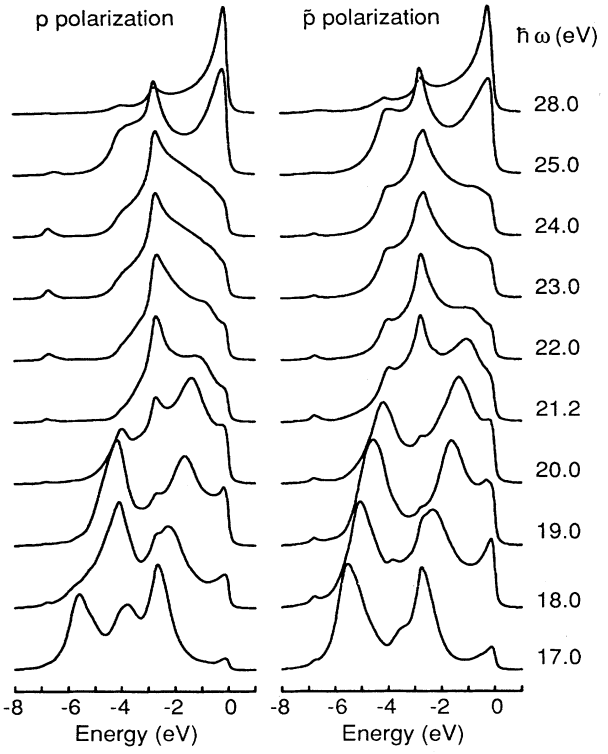

FIG. 6. Theoretical energy-distribution curves for p- (left) and $\tilde{p}$-polarized (right) radiation and normal emission. On the right the photon energy is given.

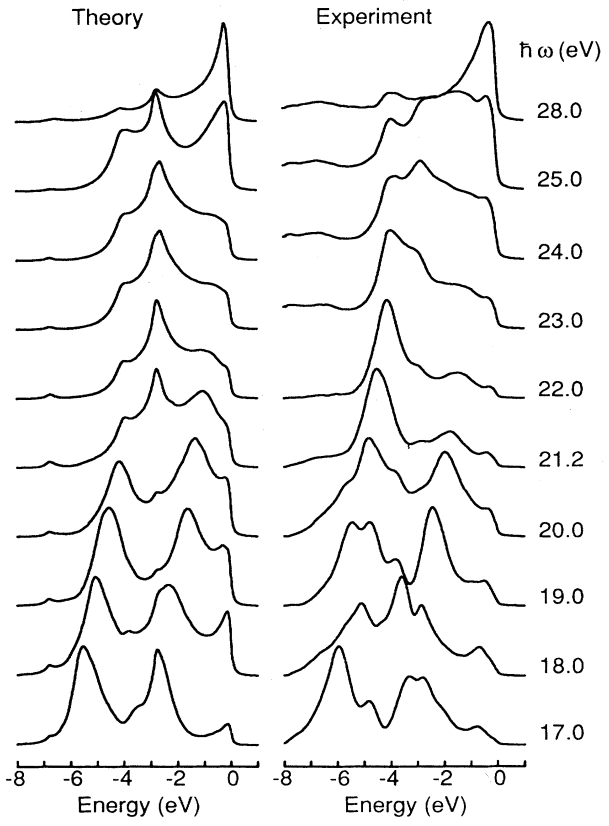

FIG. 7. Comparison of theoretical (left) and experimental (right) energy-distributions curves taken at normal emission. The photon energy is noted at the right of each experimental EDC; $\tilde{p}$ polarization is assumed.

comparably small intensity in the EDC's, as is evident from the results quoted in Sec. IV A. If the parallel component of the wave vector becomes larger some of these resonances are dispersing into the bulk band gaps and thus have to be located at the first few surface layers. Especially the dangling-bond surface state A_5 is strongly located at the outermost crystal layer, its charge density extending into the vacuum region. Therefore, the intensity of the photocurrent shows a strong dependence on the position of the detector and on incidence angles of the radiation, too.[3]

The experimental spectra have been taken with unpolarized He I radiation, and no inelastic background has been subtracted. For a fixed polar angle of the detector there have been four different measurement arrangements, which are listed in Table I. In the geometries 2 and 3 the excited electrons are detected in the direction of the unoccupied dangling-bond surface state C_3, in the remaining geometries they are leaving the crystal in the direction of the occupied surface state A_5. At incidence angles $\varphi_{\mathbf{A}}$ of 90°, $\mathbf{A}$ being the vector potential, the radiation impinges nearly perpendicular to the axis of its charge-density distribution onto the sample. In theory the vacuum-crystal interface plane lies at $z_0 = 3.69a/4$.

Theoretical and experimental energy-distribution curves are shown in Fig. 8. The first remarkable fact is that in theory as well as in experiment emissions from the dangling-bond surface state A_5 are dominating only in the spectra taken in arrangement 4. One expects that in arrangement 1, where the vector potential of the incident radiation is aligned along the wave-vector component $\mathbf{k}_{\|}$ and points along the direction of the charge distribution of the dangling-bond surface state A_5, the highest intensity should be observed. In the other measurement arrangements only a comparably weak structure is found at that energy. Additionally, one notices that in the theoretical spectra for the geometries 1 and 3 a distinct maximum at −6.1 eV can be observed. This behavior also exists in the experimental EDC's, though the comparison with the theoretical ones is rendered more difficult due to the inelastic background. The experimentally determined spectra taken at the geometries 2 and 3 are very similar, with the exception that the profile in the energy range from −2.0 eV up to the VBM differs slightly. We find the same in the corresponding theoretical EDC's including the peak at −2.0 eV, which is due to a bulk transition.

Altogether theory and experiment compare quite well.

TABLE I. Measurement arrangements for studying the polarization dependence of spectra taken at the non-normal emission presented in Fig. 8. Listed are the azimuth φ of the detector as well as the azimuth $\varphi_{\mathbf{A}}$ and the polar angle $\vartheta_{\mathbf{A}}$ of the incident radiation.

Arrangement	φ	$\varphi_{\mathbf{A}}$	$\vartheta_{\mathbf{A}}$
1	270°	90°	32°
2	90°	90°	64°
3	90°	270°	32°
4	270°	270°	64°

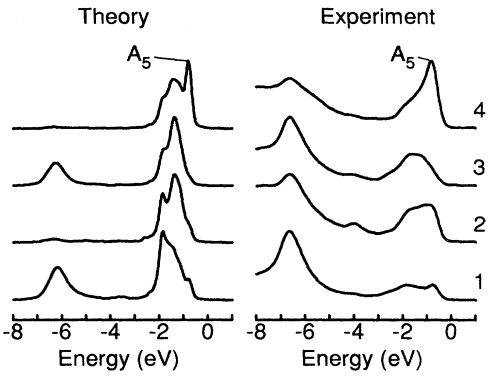

FIG. 8. Comparison of theoretical (left) and experimental (right) photoemission spectra taken with He I radiation near the point $\overline{X}'$, the polar angle of the detector being 16°. The measuring arrangement is given at the right, cf. Table I. Additionally, the dangling-bond surface state A_5 is indicated.

Exceptions seem to be the intensity ratios of the structure at −6.1 eV and transitions near the VBM, the latter being more pronounced in theory. At initial energies from −5.0 eV to −2.5 eV emissions are comparably weak in both theory and experiment.

The theoretical results presented above cannot be interpreted using only a single free-electron parabola as final state.[46] This may be seen at once applying a very simple theory of photoemission by writing the dangling-bond wave function $|\Psi_{\mathrm{db}}\rangle$ as a superposition of p_y and p_z orbitals,

$$|\Psi_{\mathrm{db}}\rangle = c_y\ |p_y\rangle + c_z\ |p_z\rangle. \tag{20}$$

The final state $|\Psi_f\rangle$ is approximated by

$$\langle \mathbf{r} \mid \Psi_f\rangle = \exp(i\mathbf{k}\cdot\mathbf{r}), \tag{21}$$

where $\mathbf{k}$ lies here in the second bulk Brillouin zone due to an umklapp process. The intensity of the photocurrent is proportional to the square of the transition-matrix element M, which reads

$$|M|^2 = |\mathbf{A}\cdot\mathbf{k}|^2\{|c_y\langle\mathbf{k}\mid p_y\rangle|^2 + |c_z\langle\mathbf{k}\mid p_z\rangle|^2 + 2\,\mathrm{Re}\,c_y^* c_z\langle\mathbf{k}\mid p_y\rangle^*\langle\mathbf{k}\mid p_z\rangle\}. \tag{22}$$

In that equation it is remarkable that the intensity between the arrangements 1 and 4 as well as in 2 and 3 varies with the same factor $|A_\perp k_\perp + A_y k_y|^2/|A_\perp k_\perp - A_y k_y|^2$ provided equal polar angles, A_y being a positive chosen amplitude factor. An analysis of the absolute intensity of the theoretical EDC's reveals that this approximation does not hold as it is also obvious from the experiment. Although the bulk conduction band 7 is coupling very strong to the outgoing wave even in non-normal emission one has to describe the final state of photoemission as well as the transition-matrix elements correctly by including the whole set of contributing conduction-band states. For example, one has to consider the boundary conditions at the surface. Thus, the statements of Huijser, van Laar,

and van Rooy[3] concerning a failure of a simple matrix-element estimation with the assumption of a single free-electron parabolic final state are confirmed theoretically.

C. Surface barrier

The discussion of the photocurrent is incomplete as long as the influence of the surface-barrier potential on the theoretical EDC's is not regarded. Here we consider especially the outgoing state to determine its dependence on the shape of the solid-vacuum interface. This modifies the coupling coefficients inherent in its expansion into bulk states and into plane waves in the vacuum region, see Eqs. (7) and (9). The respective modification of the matrix-element integration is left out at this stage because it raises CPU time requirements essentially. By this procedure only the intensities may be altered; peak positions remain unchanged.

In Fig. 9 we give a visual impression of the corrugated surface-barrier potential. The relaxation in the range of the two outermost layers leads to a slight asymmetry of the maxima in direction normal to the surface. The arsenic atoms are located at the hollow sites, but one has to keep in mind that those of the first layer are displaced in a lateral direction and, therefore, are not lying in the represented plane. The lateral mean presented in Fig. 10 shows a nearly linear ascent as in the case of metals. In the range from $2.7a/4$ to $3.1a/4$ one observes a gentle slope, which is due to the relaxation.

The parameters for the smooth barrier suggested by Manghi read $z_c = 2.84a/4$, $z_{\rm im} = 3.63a/4$, and $z_v = 4.70a/4$, the origin located at the third unrelaxed crystal layer. The steplike barrier potential chosen for comparison of the EDC's presented below is placed at $3.61a/4$ with respect to the origin and possesses the same height as the smooth barrier. We have investigated the effect of the step position on the EDC's and observed no significant changes.

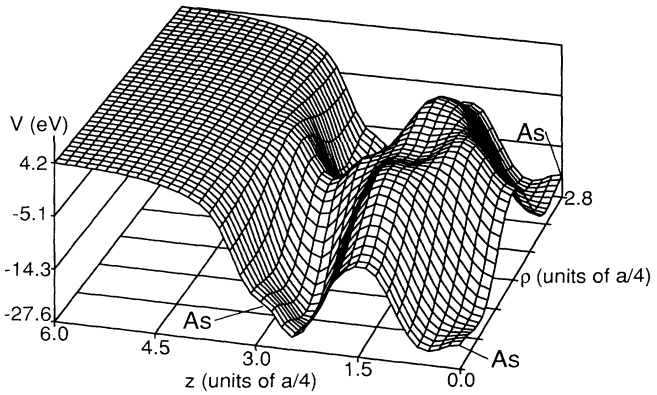

FIG. 9. Potential of the (110) surface in the range of the first two crystal layers and the solid-vacuum interface. The coordinates perpendicular and parallel to the surface are denoted z ([110] direction) and ϱ ([1$\bar{1}$0] direction), respectively. Positions of As atoms of the third and the first layer are indicated. The parameter set for the surface barrier has been taken from Ref. 44.

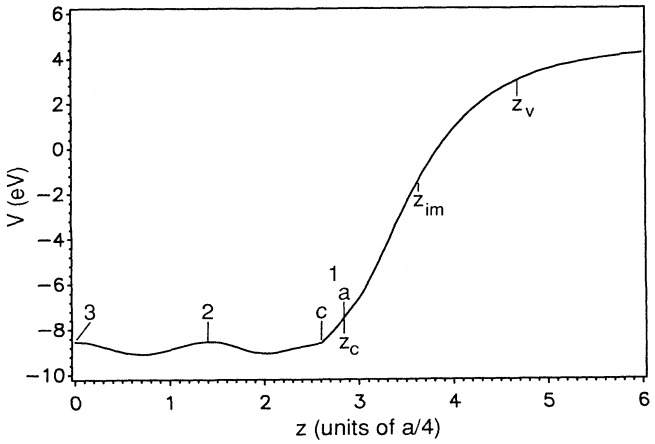

FIG. 10. Lateral mean of the (110) surface for the parameter set taken from Ref. 44, the parameters labeled z_c, $z_{\rm im}$, and z_v, cf. Eq. (18). The crystal layers are marked by numbers; a and c point onto the anion and cation located at the first layer. These are separated in the z direction due to the relaxation. The indication of the shift in the second layer is omitted.

As an example we show in Fig. 11 spectra computed for 17-eV photon energy and different measuring arrangements. The azimuth of the detector corresponds to wave vectors near the point $\overline{X}'$. The coordinate of the vacuum-crystal interface z_0 entering the transition-matrix elements is set to infinity. In all spectra the back-bond surface state A_4 shows a significant maximum in intensity, its energy being -1.1 eV. One generally notices that

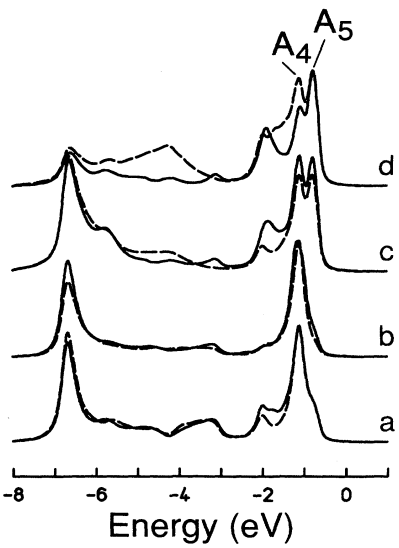

FIG. 11. Comparison of non-normal emission spectra for a smooth barrier (solid lines) and a steplike barrier (dashed lines) calculated for 17-eV photon energy and $\vartheta_{\rm A}$ being 45°. The detector azimuth ϑ is 18°. The other parameters of the series a, b, c, and d are ($\varphi = 90°$, $\varphi_{\rm A} = 90°$), (90°, 270°), (270°, 90°), and (270°, 270°). Emissions from the back bond A_4 and from the dangling bond A_5 are marked. Spectra have been normalized to equal maximum intensity.

only the energy range from −2.0 eV up to −1.5 eV is affected by the different barrier shapes, i.e., the smooth and the steplike barrier. An exception is the energy range from about −6 eV up to −4 eV for the measurement arrangement *d*. The remaining parts of the spectra are left nearly unchanged. In geometries *c* and *d* the dangling-bond surface state A_5 shows large intensity. In case *c* the smooth barrier increases the photocurrent in the energy range mentioned above with respect to the steplike potential shape. In the other case, *d*, one observes the opposite behavior.

For normal emission we have performed similar calculations, including a variety of smooth barrier shapes as well as a one-step barrier. In contrast to the case of non-normal emission we found more subtle changes in the EDC's confirming that surface-located states may be more affected by the barrier shape than bulk located ones. Both ascent and corrugation lead to significant changes in the spectra.

To conclude, the behavior of the intensity with potential shape is not clear, often ambiguous, and could not be embraced in simple terms. Thus, it may be neglected in a first examination as long as the direct effect on the matrix elements is disregarded ($z_0 = \infty$). The latter are quite important, as we have shown in Sec. IV A. However, there are some typical examples, as shown by the EDC's for arrangements *c* and *d* in Fig. 11. We found that the surface barrier shows an effect on the EDC's also at other excitation energies, i.e., in the range $\hbar\omega \leq 20$ eV. One observes changes in the intensity of significant structures, for example, surface states are affected in non-normal emission. The comparison between theory and experiment does not approve the determination of the parameters describing the barrier, but the overall best agreement is given by the chosen parameter set. Surely, the steplike barrier is not a good approximation, as is also evident from a TCS analysis.[14]

V. CONCLUSIONS

In this paper we have presented new calculations of energy-distribution curves examining some aspects of the photoemission from GaAs(110). Our theory[4] has been developed further and now includes the correct boundary condition of the final state at the surface, transition-matrix elements with surface corrections, and the effect of the surface barrier.

We have illustrated that the truncation of the solid leads to a significant effect on the transition-matrix elements, which arises from the different expansion of the final state in both half-spaces, e.g., crystal and vacuum. Small changes in the coordinate of the interface plane show distinct effects on the energy-distribution curves, allowing a determination of this important parameter inherent in our theory. The value giving the best agreement between theoretical and experimental spectra can be associated with the half-step height of the saturated image potential barrier.

The energy-distribution curves strongly depend on the incidence angles of the radiation. In the case of non-normal emission the spectra also depend drastically on the escape angles of the photoelectrons, although the corresponding wave vectors are equivalent in the surface Brillouin zone. Especially surface states with a directed charge distribution are concerned, e.g., the dangling-bond A_5 shows the most intensity if the escape direction of the photoelectrons as well as the incidence direction of the radiation are chosen to be aligned along the orientation of its charge distribution.

The surface barrier has to be taken into account to improve the agreement between experiment and theory. Although the determination of the specified potential shape fails due to the remaining differences between the spectra, a smooth saturated image potential barrier is favored by our analysis.

Our analysis shows how the computation of energy-distribution curves may close the gap between the experiment and usual band-structure calculations. It is possible to study selected effects on the theoretical spectra taking into account the intensity as well as the energy position of the structures.

The still remaining differences between the theoretical and the experimental spectra recommend further completions of the photoemission theory presented here. Firstly, the transition-matrix elements have to be calculated with the true final-state wave function within the surface-barrier region. Secondly, the photon field is not spatially constant at the surface as assumed in this paper, and thus has to be calculated microscopically. As found for the layered crystal $1T$-TiS_2 it may influence the photoemission spectra considerably.[47] Thirdly, one has to look for a still better description of the conduction-band structure, as it seems to be responsible for deviations of the energy position of the theoretical transitions from the experimentally determined ones.

ACKNOWLEDGMENTS

We would like to thank J.-V. Peetz for the valuable collaboration. The numerical computations have been performed at the Höchstleistungsrechenzentrum at Jülich and at the Rechenzentrum der Universität Kiel. The work was financially supported by the Deutsche Forschungsgemeinschaft, Contract No. Scha 360/2-2.

APPENDIX A: COMPUTER PROGRAMS

For the computation of the intensity of the photocurrent we have developed a package of several computer programs. The approximately 14 000 lines of source code are written in ANSI-FORTRAN 77, allowing us to run the package on a lot of different machines and different operating systems without any changes in the source codes.

As a first step of the calculation we compute a spline interpolation of the Fourier coefficients $V_{\mathbf{g}}(z)$ in the range of the surface barrier. In the second step the complex bulk-band structure in the conduction-band regime is calculated. Additionally, the propagator matrix is determined by direct integration of the Schrödinger equation using subroutines developed by Shampine and Gordon[48] utilizing an Adams method with variable step size. Fi-

nally, the expansion coefficients t_i and $\phi_{\mathbf{g}}$ are calculated by the wave-function-matching procedure. In the last stage transition-matrix elements and the Green's function of the semi-infinite solid are computed. All these quantities are subsequently combined to yield the photocurrent. Because of the large amount of necessary computer time most of the data are stored in disk files and thus have to be computed only once.

In the last stage of our analysis the programs sketched above were running on a CRAY YMP-8 32 computer. The computation of the final state requires 35-sec execution time per energy and parallel component of the wave vector and 2.5 MWords (1 Word =8 Bytes) of storage. The evaluation of the intensities needs approximately 2500 sec per EDC.

APPENDIX B: FOURIER TRANSFORMATION OF ATOMIC ORBITALS INCLUDING THE SURFACE

In this appendix a very short sketch of the calculation of the Fourier-transformed orbitals is given. The atomic orbitals used in the LCAO scheme are linear combinations of Slater orbitals. Thus, only the latter are involved in the calculation of the Fourier transformation and we are concerned with integrals of the form

$$I(\mathbf{k}) = \int_{\mathcal{R}^2} dx\,dy \int_{-\infty}^{z_0} dz\ \exp(i\mathbf{k}\cdot\mathbf{r} - \lambda r)\ r^n\, Y_{lm}[\Omega(\mathbf{r})]$$

for angular momenta $l = 0, 1$ and Ω denoting the solid angle. $\mathrm{Im}\, k_\perp$ is less equal to zero because the final state is decaying towards the bulk, i.e., in the $-z$ direction.

As a first step we introduce the Fourier transform of the Heaviside step function $\Theta(z_0 - z)$ allowing us to extend the integration over the whole space, for which we have to pay by an additional integral. With $\boldsymbol{\kappa} = (\mathbf{k}_\parallel, k_\perp + s)$, s being the conjugate variable to z, one gets immediately

$$I(\mathbf{k}) = \frac{i}{2\pi}\int_{-\infty}^{+\infty} ds\ \frac{1}{s}\exp(-isz_0)\ J(\boldsymbol{\kappa}),$$

where $J(\boldsymbol{\kappa})$ is the Fourier-transformed Slater orbital without surface, i.e., $z_0 = +\infty$, which is already known.[39]

For orbitals with s symmetry we have

$$\begin{aligned} I(\mathbf{k}) = {} & \frac{i}{2\sqrt{\pi}}(n+1)! \\ & \times \int ds\ \exp(-isz_0)\frac{1}{is\kappa} \\ & \times \left\{(\lambda - i\kappa)^{-(n+2)} - (\lambda + i\kappa)^{-(n+2)}\right\} \end{aligned}$$

with $\kappa = \sqrt{\boldsymbol{\kappa}\cdot\boldsymbol{\kappa}}$. Applying the binomial theorem one arrives at

$$I(\mathbf{k}) = \frac{i}{\sqrt{\pi}}(n+1)!\sum_{p=0}^{[\frac{n+1}{2}]}\binom{n+2}{2p+1}\lambda^{n+1-2p}\ K(p),$$

where $K(p)$ is defined as

$$K(p) = \int ds\ \ \exp(-isz_0)\frac{1}{s}(i\kappa)^{2p}(\lambda^2+\kappa^2)^{-(n+2)},$$

and square brackets denote the maximum integer less equal to its argument. This remaining integral can be solved by the residual theorem. The poles of the integrand are $s_1 = 0$, $s_{2,3} = -k_\perp \pm i\sqrt{\mathbf{k}_\parallel^2 + \lambda^2}$, where the first is of order 1 and the latter are of order $n+2$. The calculation of the residues is straightforward; in the cases of s_2 and s_3 the extended Leibniz product rule is used. Finally, one arrives at expressions which can be easily transferred into efficient FORTRAN source code. A short form of the result is

$$\begin{aligned} I(\mathbf{k}) = {} & \frac{i}{\sqrt{\pi}}(n+1)!\sum_{p=0}^{[\frac{n+1}{2}]}\binom{n+2}{2p+1}\lambda^{n+1-2p} \\ & \times(-2\pi i)\ [\mathrm{Res}(s_1,p) + \mathrm{Res}(s_3,p)] \end{aligned}$$

for $z_0 \geq 0$ and

$$\begin{aligned} I(\mathbf{k}) = {} & \frac{i}{\sqrt{\pi}}(n+1)!\sum_{p=0}^{[\frac{n+1}{2}]}\binom{n+2}{2p+1}\lambda^{n+1-2p} \\ & \times 2\pi i\ \mathrm{Res}(s_2,p) \end{aligned}$$

for $z_0 \leq 0$. We note that the terms with the residue for s_1 give just the result for $z_0 = +\infty$; the remaining ones represent the cutoff due to the surface.

The Slater orbitals with p symmetry are treated in the same way, the expressions a little more complicated because of the Fourier transformed $J_\sigma(\boldsymbol{\kappa}), \sigma \in \{x, y, \perp\}$, which read

$$\begin{aligned} J_\sigma(\boldsymbol{\kappa}) = {} & \frac{2\pi i}{\kappa}\ n! Y_\sigma(\Omega(\boldsymbol{\kappa})) \\ & \times\left[(\lambda - i\kappa)^{-(n+1)}\left(\frac{1}{i\kappa} - \frac{n+1}{\lambda - i\kappa}\right)\right. \\ & \left. - (\lambda + i\kappa)^{-(n+1)}\left(\frac{1}{i\kappa} + \frac{n+1}{\lambda + i\kappa}\right)\right]. \end{aligned}$$

Spherical harmonics for complex argument have been discussed by Olver.[49] Writing the total integral $I(\mathbf{k})$ as

$$I(\mathbf{k}) = I_1(\mathbf{k}) - I_2(\mathbf{k}),$$

we arrive at

$$\begin{aligned} I_1(\mathbf{k}) = {} & -2n!\sum_{p=0}^{[n/2]}\binom{n+1}{2p+1}\lambda^{n-2p} \\ & \times(-1)^p K(n+1,p,\sigma) \end{aligned}$$

$$\begin{aligned} I_2(\mathbf{k}) = {} & -2(n+1)!\sum_{p=0}^{[(n+2)/2]}\binom{n+2}{2p}\lambda^{n+2-2p} \\ & \times(-1)^p\ K(n+2,p,\sigma), \end{aligned}$$

with $K(n,p,\sigma)$ defined as

$$\begin{aligned} & K(n,p,\sigma) \\ & = \sqrt{\frac{3}{4\pi}}\int_{-\infty}^{+\infty} ds\frac{1}{s\kappa}\ \frac{\kappa_\sigma}{\kappa}(\lambda^2+\kappa^2)^{-n}\kappa^{2p}\ \exp(-isz_0). \end{aligned}$$

The poles of the integrand are s_1, s_2, and s_3, the same as for orbitals with s symmetry. Thus, the remaining task is to evaluate the residues of $K(n,p,\sigma)$ which is straightforward.

*Present address: Universität Duisburg-GH, Theoretische Festkörperphysik, D-4100 Duisburg, Federal Republic of Germany.
†Present address: Institut für neue Materialien, Universität des Saarlandes, Gebäude 43, D-6600 Saarbrücken, Federal Republic of Germany.

[1]G. V. Hansson and R. I. G. Uhrberg, Surf. Sci. Rep. **9**, 197 (1988) and references therein.
[2]G. P. Williams, F. Cerrina, G. J. Lapeyre, J. R. Anderson, R. J. Smith, and J. Hermanson, Phys. Rev. B **34**, 5548 (1986).
[3]A. Hiujser, J. van Laar, and T. L. van Rooy, Phys. Lett. **65A**, 337 (1978).
[4]J. Henk, W. Schattke, H.-P. Barnscheidt, C. Janowitz, R. Manzke, and M. Skibowski, Phys. Rev. B **39**, 13 286 (1989).
[5]J. Olde, G. Mante, H.-P. Barnscheidt, L. Kipp, J.-C. Kuhr, R. Manzke, M. Skibowski, J. Henk, and W. Schattke, Phys. Rev. B **41**, 9958 (1990).
[6]J. Olde, K.-M. Behrens, H.-P. Barnscheidt, R. Manzke, M. Skibowski, J. Henk, and W. Schattke, Phys. Rev. B **44**, 6312 (1991).
[7]R. D. Bringans and R. Z. Bachrach, Phys. Rev. Lett. **20**, 1954 (1984).
[8]See, for example, G.-X. Qian, R. M. Martin, and D. J. Chadi, Phys. Rev. B **37**, 1303 (1988); M.-H. Tsai, J. D. Dow, R. P. Wang, and R. V. Kasowski, *ibid.* **40**, 9818 (1989).
[9]J. Hebenstreit, M. Heinemann, and M. Scheffler, Phys. Rev. Lett. **67**, 1031 (1991).
[10]H. Carstensen, Ph.D. thesis, Universität Kiel, 1991; C. Janowitz, Ph.D. thesis, Universität Kiel, 1991.
[11]P. J. Feibelman and D. E. Eastman, Phys. Rev. B **10**, 4932 (1974).
[12]G. D. Mahan, Phys. Rev. B **2**, 4334 (1970).
[13]T. Grandke, L. Ley, and M. Cardona, Phys. Rev. B **18**, 3847 (1978).
[14]J.-V. Peetz, W. Schattke, H. Carstensen, R. Manzke, and M. Skibowski, Phys. Rev. B **46**, 10 127 (1992).
[15]E. Clementi and C. Roetti, At. Data Nucl. Data Tables **14**, 177 (1974).
[16]J. R. Chelikowsky and M. L. Cohen, Phys. Rev. B **14**, 556 (1976).
[17]R. S. Mulliken, J. Chem. Phys. **23**, 1833 (1955); **23**, 1841 (1955).
[18]J. C. Phillips, Rev. Mod. Phys. **42**, 317 (1970).
[19]Y. Wang, P. Nordlander, and N. H. Tolk, J. Chem. Phys. **89**, 4163 (1988).
[20]C. Kruse, Masters thesis, Universität Kiel, 1990.
[21]M. Cardona, N. E. Christensen, and G. Fasol, Phys. Rev. B **38**, 1806 (1988).
[22]M. P. López Sancho, J. M. López Sancho, and J. Rubio, J. Phys. F **15**, 851 (1985).
[23]J. Pollmann and S. Pantelides, Phys. Rev. B **18**, 5524 (1978).
[24]L. E. Ballentine and M. Kolâr, J. Phys. C **19**, 981 (1986).
[25]J. Henk and W. Schattke, Solid State Commun. **70**, 683 (1989).
[26]M. Lehmann, Masters thesis, Universität Kiel, 1988.
[27]C. B. Duke, S. L. Richardson, A. Paton, and A. Kahn, Surf. Sci. **127**, L135 (1983).
[28]S. B. Zhang and M. L. Cohen, Surf. Sci. **172**, 754 (1986).
[29]J. L. A. Alves, J. Hebenstreit, and M. Scheffler, Phys. Rev. B **44**, 6188 (1991) and references therein.
[30]R. Manzke, H.-P. Barnscheidt, C. Janowitz, and M. Skibowski, Phys. Rev. Lett. **58**, 610 (1987).
[31]J. Hermanson, Solid State Commun. **22**, 9 (1977).
[32]M. L. Cohen and T. K. Bergstresser, Phys. Rev. **141**, 789 (1966).
[33]See, for example, H. Bross, Surf. Sci. **213**, 215 (1989).
[34]J. B. Pendry, J. Phys. C **2**, 2273 (1969).
[35]We follow the nomenclature of Y.-C. Chang, Phys. Rev. B **25**, 605 (1982). Real bands have arbitrary $\mathrm{Re}(k_\perp)$ and $\mathrm{Im}(k_\perp) = 0$, whereas imaginary bands of the first kind have $\mathrm{Re}(k_\perp) = 0$ and $\mathrm{Im}(k_\perp) \neq 0$.
[36]J. F. L. Hopkinson, J. B. Pendry, and D. J. Titterington, Comp. Phys. Commun. **19**, 69 (1980).
[37]E. Pehlke, W. Schattke, O. Anderson, R. Manzke, and M. Skibowski, Phys. Rev. B **41**, 2982 (1990).
[38]J. C. Bartling and R. A. Craig, Phys. Rev. B **3**, 3170 (1971).
[39]J. W. Gadzuk, Phys. Rev. B **10**, 5030 (1974).
[40]A. Mazur, J. Pollmann, and M. Schmeits, Solid State Commun. **42**, 37 (1982).
[41]T. P. Humphreys, G. P. Srivastava, and R. H. Williams, J. Phys. C **19**, 1259 (1986).
[42]P. M. Marcus and D. W. Jepsen, Phys. Rev. Lett. **20**, 925 (1968).
[43]See, for example, J. Rundgren and G. Malmström, J. Phys. C **10**, 4671 (1977); R. O. Jones, P. J. Jennings, and O. Jepsen, Phys. Rev. B **29**, 6474 (1984); E. Tamura and R. Feder, Z. Phys. B **81**, 425 (1990).
[44]F. Manghi, Phys. Rev. B **33**, 2554 (1986).
[45]J. Henk, J.-V. Peetz, and W. Schattke, in *The Physics of Semiconductors*, edited by E. M. Anastassakis and J. D. Joannopoulos (World Scientific, Singapore, 1990), Vol. 1, p. 175.
[46]See for additional information on this topic, N. J. Shevchik and D. Liebowitz, Phys. Rev. B **18**, 1618 (1978); D. Liebowitz and N. J. Shevchik, *ibid.* **18**, 1630 (1978).
[47]D. Samuelsen, E. Pehlke, W. Schattke, O. Anderson, R. Manzke, and M. Skibowski, Phys. Rev. Lett. **68**, 522 (1992).
[48]L. F. Shampine and M. K. Gordon, *Computerlösung gewöhnlicher Differentialgleichungen* (Vieweg, Braunschweig, 1984).
[49]F. W. J. Olver, *Asymptotics and Special Functions* (Academic, New York, 1974).